

The Photodetector Array Camera and Spectrometer (PACS) for the Herschel Space Observatory

Albrecht Poglitsch^a, Christoffel Waelkens^b, Otto H. Bauer^a, Jordi Cepa^c,
Helmut Feuchtgruber^a, Thomas Henning^d, Chris van Hoof^e, Franz Kerschbaum^f,
Dietrich Lemke^d, Etienne Renotte^g, Louis Rodriguez^h, Paolo Saracenoⁱ, and
Bart Vandenbussche^b

^aMax-Planck-Institut für extraterrestrische Physik, Postfach 1312, 85741 Garching, Germany

^bKatholieke Universiteit Leuven, Celestijnenlaan 200B, 3001 Leuven, Belgium

^cInstituto de Astrofísica de Canarias, C/Via Lactea s/n, La Laguna,
38200 Santa Cruz de Tenerife, Spain

^dMax-Planck-Institut für Astronomie, Königstuhl 17, 69117 Heidelberg, Germany

^eInteruniversity Microelectronics Center, Kapeldreef 75, 3001 Leuven, Belgium

^fInstitut für Astronomie der Universität Wien, Türkenschanzstraße 17, 1180 Wien, Austria

^gCentre Spatial de Liège, Parc Scientifique du Sart Tilman, Avenue du Pré-Aily,
4031 Angleur-Liège, Belgium

^hCommissariat à l'Énergie Atomique, Service d'Astrophysique, Orme des Merisiers, Bât. 709,
91191 Gif/Yvette, France

ⁱIstituto di Fisica dello Spazio Interplanetario, Via del Fosso del Cavaliere, 00133 Roma, Italy

ABSTRACT

The Photodetector Array Camera and Spectrometer (PACS) is one of the three science instruments for ESA's far infrared and submillimeter observatory Herschel. It employs two Ge:Ga photoconductor arrays (stressed and unstressed) with 16×25 pixels, each, and two filled silicon bolometer arrays with 16×32 and 32×64 pixels, respectively, to perform imaging line spectroscopy and imaging photometry in the $60 - 210\mu\text{m}$ wavelength band. In photometry mode, it will simultaneously image two bands, $60 - 85\mu\text{m}$ or $85 - 130\mu\text{m}$ and $130 - 210\mu\text{m}$, over a field of view of $\sim 1.75' \times 3.5'$, with full beam sampling in each band. In spectroscopy mode, it will image a field of $\sim 50'' \times 50''$, resolved into 5×5 pixels, with an instantaneous spectral coverage of ~ 1500 km/s and a spectral resolution of ~ 175 km/s. In both modes the performance is expected to be not far from background-noise limited, with sensitivities (5σ in 1h) of ~ 4 mJy or $3 - 20 \times 10^{-18} \text{W/m}^2$, respectively.

We summarize the design of the instrument and its subunits, describe the observing modes in combination with the telescope pointing modes, report results from instrument level performance tests of the Qualification Model, and present our current prediction of the in-orbit performance of the instrument based on tests done at subunit level.

Keywords: Instruments: far infrared; instruments: space; instruments: photometer, integral field spectrometer; missions: Herschel

1. INTRODUCTION

The far infrared and submillimetre satellite Herschel will open up the wavelength range $60 - 600\mu\text{m}$ to photometry and spectroscopy with unprecedented sensitivity and spatial resolution, unobscured by the Earth's atmosphere.

Within the complement of three instruments selected to form the science payload, the shortest wavelength band, $60 - 210\mu\text{m}$, will be covered by the Photodetector Array Camera & Spectrometer (PACS), which will

Further author information: (Send correspondence to A.P.)

A.P.: E-mail: alpog@mpe.mpg.de, Telephone: +49 89 30 000 3293

provide both photometric and spectroscopic observing modes suited to address the key scientific topics of the Herschel mission.

2. INSTRUMENT DESIGN AND SUBUNITS

The requirements leading to the design of PACS have been discussed previously;¹ here we briefly summarize the instrument concept. The instrument will offer two basic modes in the wavelength band 60 – 210 μm :

- Imaging dual-band photometry (60 – 85 μm or 85 – 130 μm and 130 – 210 μm) over a field of view of 1.75' \times 3.5', with full sampling of the telescope point spread function (diffraction/wavefront error limited)
- Integral-field line spectroscopy between 57 and 210 μm with a resolution of \sim 175 km/s and an instantaneous coverage of \sim 1500 km/s, over a field of view of 47'' \times 47''

Both modes will allow spatially chopped observations by means of an instrument-internal chopper mirror with variable throw; this chopper is also used to alternatively switch two calibration sources into the field of view.

The focal plane sharing of the instrument channels is shown in Fig. 1. The photometric bands, which can be observed simultaneously, cover the same field of view, while the field of view of the spectrometer is offset from

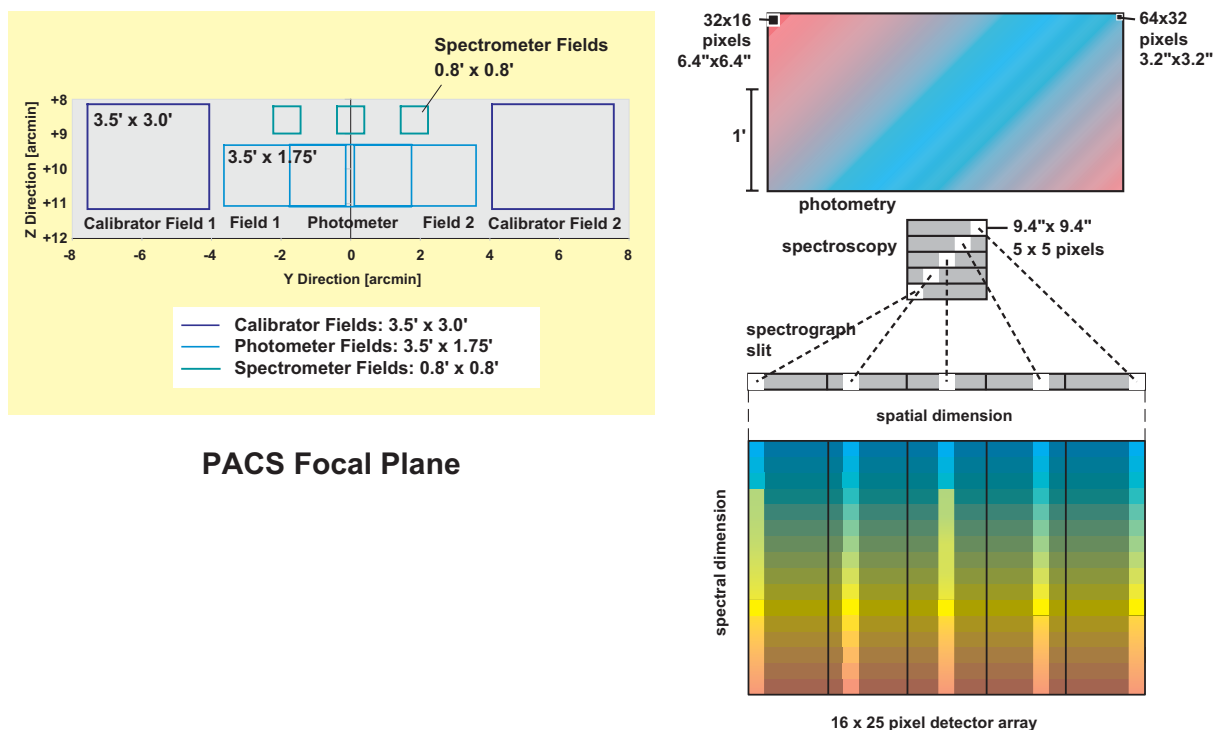


Figure 1. Left: PACS focal plane usage. Long-wavelength and short-wavelength photometry bands cover identical fields of view. The spectrometer field of view is offset in the -z direction. Chopping is done along the y axis (left-right in this view) and also allows observation of the internal calibrators on both sides of the used area in the telescope focal plane. The chopper throw for sky observations is $\pm 1/2$ the width of the photometer field such that object and reference fields can be completely separated (photometer field 1 and 2). Right: focal plane footprint. A fixed mirror is used to split the focal plane into the photometry and spectroscopy channels of the instrument. In the photometry section, the two wavelength bands are simultaneously imaged with different magnification to reach full beam sampling in both bands. In the spectroscopy section, an optical image slicer re-arranges the 2-dimensional field along the entrance slit of the grating spectrograph such that, for all spatial elements in the field, spectra are observed simultaneously.

the photometer field (Fig. 1). Since photometry and spectroscopy operation are mutually exclusive this has no effect on the observing efficiency. The focal plane unit provides these capabilities through five functional units:

- common input optics with the chopper, calibration sources and a focal plane splitter
- a photometer optical train with a dichroic beam splitter and separate re-imaging optics for the short-wavelength bands ($60 - 85\mu\text{m}$ / $85 - 130\mu\text{m}$) and the long-wavelength band ($130 - 210\mu\text{m}$), respectively; band-defining filters on a wheel select one of the two short-wavelength bands at a time
- a spectrometer optical train with an image slicer unit for integral field spectroscopy, an anamorphic collimator, a diffraction grating in Littrow mount with associated actuator and position readout, anamorphic re-imaging optics, and a dichroic beam splitter for separation of diffraction orders
- 2 bolometer arrays with cryogenic buffers/multiplexers and a common 0.3 K sorption cooler
- 2 photoconductor arrays with attached cryogenic readout electronics (CRE).

All subunits have been described in more detail in previous papers;^{1,2} here we only give an update on performance-relevant developments or changes.

2.1. Photoconductor Arrays

The 25×16 pixels Ge:Ga photoconductor arrays (Fig. 2) are a completely modular design. 25 linear modules of 16 pixels each are stacked together to form a contiguous, 2-dimensional array. The light cones in front of the actual detector block provide for area-filling light collection in the focal plane. Details of the design of both arrays have been published.³⁻⁶

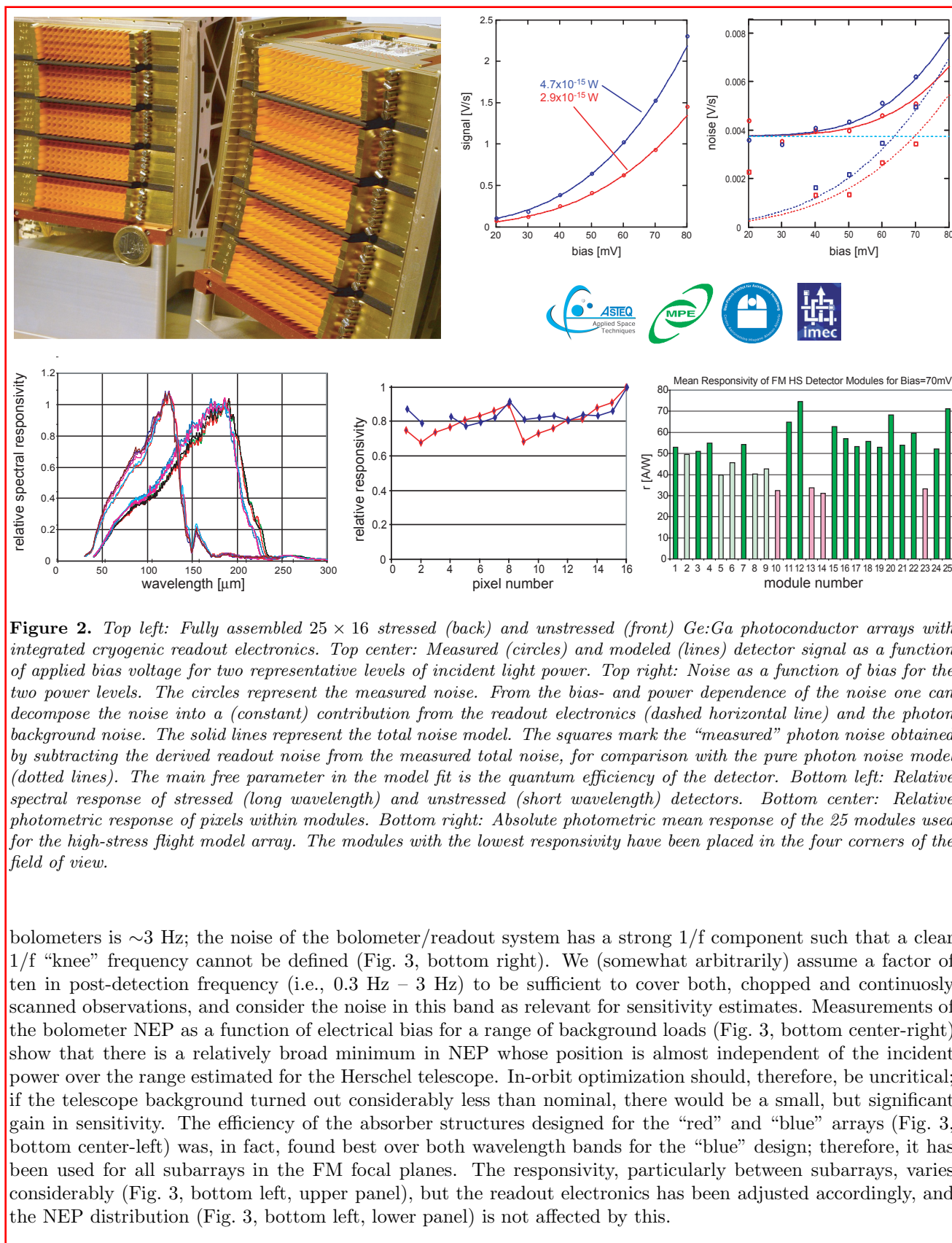
Responsivity measurements of both stressed and unstressed modules show sufficiently homogeneous spectral and photometric response within each module and between modules (Fig. 2, bottom center/right). Absolute responsivity numbers are preliminary as the optimum bias for in-orbit operation is not determined, yet. Likely numbers will be $\sim 10\text{A/W}$ for the unstressed detectors and $\sim 40\text{A/W}$ for the stressed detectors.

Each linear module of 16 detectors is read out by a cryogenic amplifier/multiplexer circuit (CRE) in CMOS technology.^{7,8} Based on the experience with the Qualification Model, a new generation of CREs has been developed for the Flight Model. With this circuit, which has reduced parasitic capacitance at its inputs, the input current noise density has been further reduced compared to the QM. The readout electronics is integrated into the detector modules.

Measurements on FM detectors have been carried out to optimize their operation and to allow a prediction of their in-orbit performance. Some of these measurements were suited to separate the readout electronics noise from the intrinsic photon detection process (Fig. 2, top center/right). These measurements can be consistently described by a constant contribution in current noise density from the CREs and a noise component proportional to the photon background noise, where this proportionality can be expressed in terms of an (apparent) quantum efficiency, with a peak value of 26%.

2.2. Bolometer Arrays

The PACS bolometers are filled arrays of square pixels which allow instantaneous beam sampling. 4×2 monolithic sub-arrays of 16×16 pixels are tiled together to form the short-wave focal plane array (Fig. 3, top center). In a similar way, 2 sub-arrays of 16×16 pixels are tiled together to form the long-wave focal plane array. The subarrays are mounted on a 0.3 K carrier which is thermally isolated from the surrounding 2 K structure. The buffer/multiplexer electronics is split in two levels; a first stage is part of the indium-bump bonded back plane of the focal plane arrays, operating at 0.3 K. Ribbon cables connect the output of the 0.3 K readout to a buffer stage running at 2 K. The multiplexing readout samples each pixel at a rate of 40 Hz or 20 Hz. Details on the bolometer design are given elsewhere.⁹⁻¹¹ Both array assemblies are mounted in a subunit of the FPU (Fig. 3, top right) together with the 0.3 K cooler¹² which provides uninterrupted operation for two days, with a typical hold time of 59 hours measured in our lab cryostat. The post-detection bandwidth (thermal/electrical) of the



bolometers is ~ 3 Hz; the noise of the bolometer/readout system has a strong $1/f$ component such that a clear $1/f$ “knee” frequency cannot be defined (Fig. 3, bottom right). We (somewhat arbitrarily) assume a factor of ten in post-detection frequency (i.e., 0.3 Hz – 3 Hz) to be sufficient to cover both, chopped and continuously scanned observations, and consider the noise in this band as relevant for sensitivity estimates. Measurements of the bolometer NEP as a function of electrical bias for a range of background loads (Fig. 3, bottom center-right) show that there is a relatively broad minimum in NEP whose position is almost independent of the incident power over the range estimated for the Herschel telescope. In-orbit optimization should, therefore, be uncritical; if the telescope background turned out considerably less than nominal, there would be a small, but significant gain in sensitivity. The efficiency of the absorber structures designed for the “red” and “blue” arrays (Fig. 3, bottom center-left) was, in fact, found best over both wavelength bands for the “blue” design; therefore, it has been used for all subarrays in the FM focal planes. The responsivity, particularly between subarrays, varies considerably (Fig. 3, bottom left, upper panel), but the readout electronics has been adjusted accordingly, and the NEP distribution (Fig. 3, bottom left, lower panel) is not affected by this.

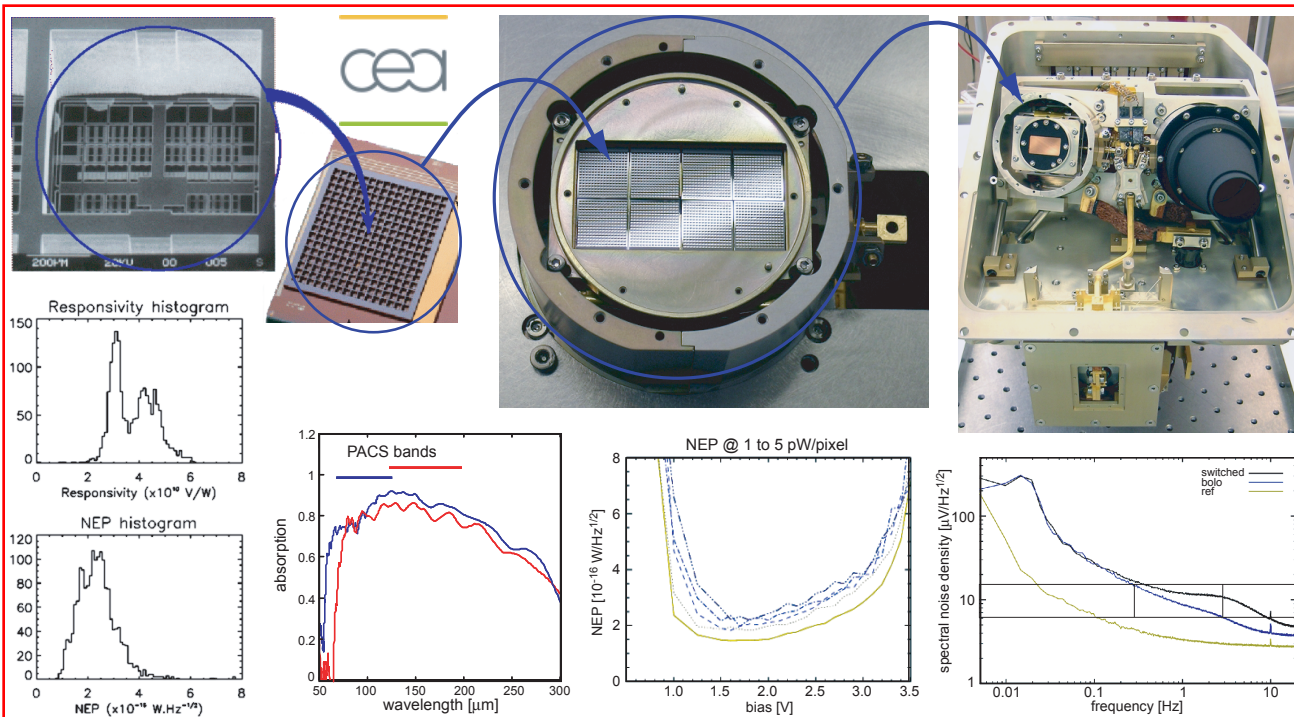


Figure 3. Top left: Micrograph of one pixel of the filled bolometer array next to a photo of a 16×16 pixels subarray. The physical size of a PACS pixel is 0.75 mm. The absorber and back-reflector grids as well as the integrated thermistor are monolithic silicon structures. Top center: 4×2 subarrays form the focal plane of the FM short-wave bolometer assembly. The 0.3 K focal plane is suspended from its 2 K enclosure by Kevlar strings. Close to the right edge of the picture, the thermal interface to the 0.3 K cooling bar is visible. Top right: Photometer focal plane unit (FM) with the two bolometer assemblies (short-wave, baffle cone removed / long-wave, with baffle cone) and the 0.3 K sorption cooler. A Kevlar-suspended cooling bar provides the thermal connection from the cold tip of the cooler to the 0.3 K interfaces of the bolometer assemblies. Bottom left: Responsivity and NEP histograms of the short-wave bolometer array under nominal background illumination. Bottom center-left: Efficiency of the short-wave and long-wave bolometer absorber structures. The horizontal bars mark the wavelength ranges of the PACS bands. Bottom center-right: NEP as a function of detector bias for a range of background levels. Bottom right: Electrical noise spectra of the bare multiplexer (bottom) and of the detector/multiplexer in simple readout mode (middle) and in “double-correlated” readout mode (top).

3. OBSERVING MODES AND AOTS

The observing modes supported by PACS are combinations of *instrument modes* and *satellite pointing modes*. They are accessible to the observer through Astronomical Observation Templates (AOT) which are “filled out” through a graphical user interface, HSpot. Three different AOTs have been defined and implemented to perform astronomical observations with PACS; one generic for the photometer and two for the spectrometer. All further details of the observation are defined as parameters within the AOT through HSpot. Regular integration periods on the internal calibration sources are inserted automatically. It should be noted that AOTs are in the process of definition and will undergo further optimization.

3.1. Photometer

Three observing modes are offered with the photometer AOT:

1. Point source photometry: This mode is targeted at observations of sources which are completely isolated and point-like or smaller than one blue matrix. A typical use of this AOT is for point-source photometry. It uses chopping and nodding, both with amplitude of 1 blue matrix, and dithering with a 1 pixel amplitude, keeping the source on the array at all times.

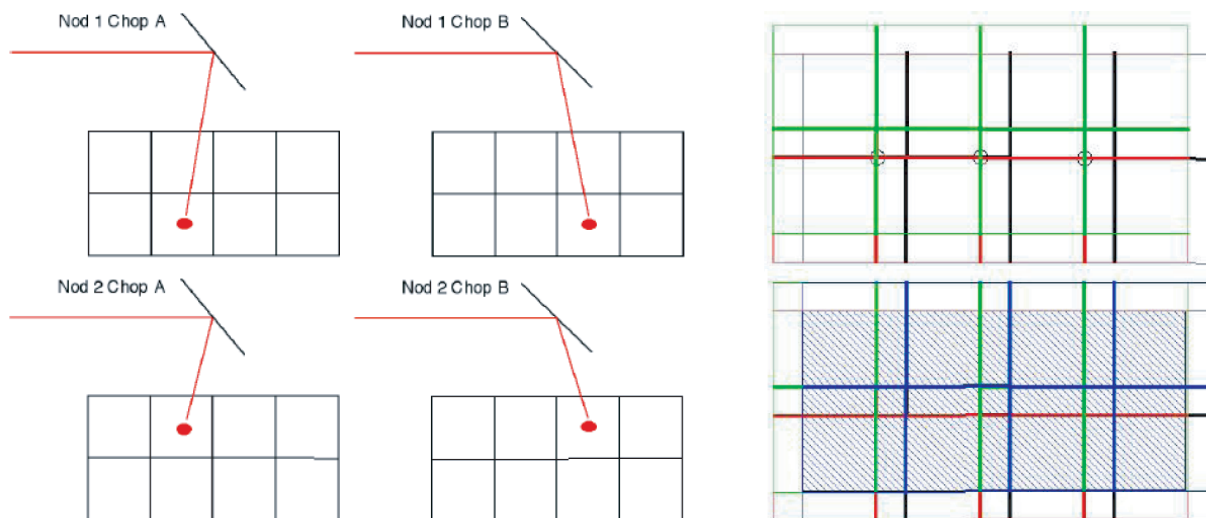


Figure 4. Left: Sketch showing the source positions as a function of the nod and chopper positions. The y-axis is horizontal, the z-axis is vertical. Chop positions are defined by the internal chopper, while nod positions are defined by the satellite pointing. Chopper positions A and B are subtracted from each other to suppress the background and deal with possible low-frequency drifts, differences obtained in nod position 1 and 2 are subtracted from each other to remove remaining telescope/instrument gradients. Dithering at each chopper position, performed with the internal chopper, is not shown. Right: Footprint of the detector on the sky; thin lines: outline of the detector, thick lines: gaps between subarrays. The pointing sequence is color coded and goes black, red, green, blue. The top panel shows the resulting footprint after one y-axis and one z-axis motion. By the y axis motion alone, the horizontal gap between the 4 top and bottom matrices would remain blind. The z-axis motion covers almost all this area except for the three encircled pixels. A second y-axis motion, in the opposite direction to maximize the overlap area, leads to complete coverage. The completely covered area at the end of the observation is indicated as a hatched zone (bottom panel).

2. “Small source” photometry: This mode is targeted at observations of sources that are smaller than the array size, yet larger than a single matrix. To be orientation independent, this means sources that fit in $2' \times 2'$. This AOT uses chopping and nodding, but the source cannot be kept on the array at all times.
3. Large area or extended source mapping: This mode is necessary to map sources larger than the array size, or to cover large contiguous areas of the sky, e.g. extragalactic surveys. There are two ways to perform this kind of observations:
 - scanning (without chopping)
 - rastering (without chopping)

The pointing/chopping/nodding scheme of the first two modes is depicted in Fig. 4.

3.2. Line Spectroscopy

This AOT is intended to observe one or several spectral line features. Up to 10 lines can be studied within one observation. The spacecraft may be used in the staring or in the raster mode. Nodding is permitted in either pointing modes. In all cases, the use of the internal chopper is imposed by the design of the AOT. The fixed wavelength and its immediate neighborhood is observed for each chopper and grating position. For improved flat-fielding, especially for long integrations, the grating is scanned by a number of discrete steps around a specified centre position such that drifts in the detector responsivity between individual pixels are eliminated. For each user defined wavelength, PACS performs an up/down grating scan with an amplitude such that a given wavelength is seen successively by all 16 spectral pixels. After all lines have been completed, the satellite moves to a nod-position, if selected, and the lines are repeated in the same manner. The spectral sampling in this mode

is fixed to “high”, i.e., $> 3\times$ Nyquist sampling. If lines of second and third grating order are included, one or more filter switches are necessary. Depending on the requested wavelength/grating order, only the data of one of the two detector arrays is normally of interest to the observer.

Additionally, we are implementing a wavelength-switching mode that does not rely on the chopper for background subtraction; instead, successive fast scans on the line position and an adjacent wavelength are performed. The frequency switching option is very efficient, because 100% of the integration time is spent on target, and it can be used for large extended sources where off-source chopping is not possible. Caution: by definition, this technique eliminates the continuum information, and it is susceptible to confusion in spectrally crowded areas.

3.3. Range Spectroscopy

Similarly to the Line scan spectroscopy mode, this AOT allows to perform one or several spectral line features (up to ten), but the user can freely specify the explored wavelength range or choose a predefined range that will cover the entire bandwidth of PACS. The use of the internal chopper is imposed by the design of the AOT. The spacecraft may be used in staring or in raster modes. Nodding is permitted in either pointing modes. The user has two alternatives in the wavelength setting of range scan spectroscopy mode AOT in HSpot. If the option “Range Scan” is selected, a number of wavelength ranges (low and high wavelength pairs) have to be entered. Alternatively, if the option “SED” is selected, an internally defined range that covers the entire bandwidth of PACS will be covered in two distinct grating scans. For each user defined wavelength range, PACS will perform an up/down grating scan, of such an amplitude that the given bracketing wavelengths will be successively seen by all 16 “spectral” pixels. In fact, the grating excursion is slightly larger so that some baseline will be explored beyond pixels 1 and 16. The astronomer also has control over the sampling interval, in the instrument setting panel, given by the HSpot options “high” ($> 3\times$ Nyquist sampling), “medium” ($> 2\times$ Nyquist sampling) or “low” ($>$ Nyquist sampling) for “Range Scan”, and the options “fast”, “slow” or “normal” (3, 6 or 9 spectral pixels per grating step) for the SED mode.

4. INSTRUMENT LEVEL TEST RESULTS

The results presented here all refer to tests performed on the QM instrument in 2004; no tests have been performed on the flight model at instrument level, yet, at the time of this writing. We only report results with a direct impact on the (expected) performance of the FM.

4.1. Instrument Point Spread Function

Measurements of the PSF of PACS were performed in the $75\mu\text{m}$ and $110\mu\text{m}$ bands of the photometer and, using both photoconductor arrays, at wavelengths around $175\mu\text{m}$ in the first grating order and around $87\mu\text{m}$ in the second grating order (Fig. 5, left column). Point-like sources were realized by placing an external, hot blackbody source with metallic, ambient temperature hole masks in the nominal focus of our telescope simulator optics in front of the cryostat window. Due to a deviation of the as-built test cryostat from the optics design, the actual focus position was not accessible and the measurements had to be carried out with a considerable defocus. For the spectrometer tests, the S/N ratio on this source was low, even though we added up the signals from all 16 spectral channels of each spatial position. The photometer tests revealed a PSF which is $\approx 45\%$ wider than nominal at $75\mu\text{m}$ and $\approx 25\%$ wider than nominal at $110\mu\text{m}$, compatible with the nominal PSF, given the amount of defocus in the test optics. The PSF measurements of the spectrometer with its larger pixel size and lower S/N ratio show no discrepancy with respect to the photometer results and demonstrate that the integral-field optics is working as designed.

4.2. Photometer Flat Field

This test was performed with the “blue” photometer by scanning of the internal chopper over its full range, from one internal calibration source and across the astronomical field of view to the other calibration source. The astronomical field was illuminated by either of the two cryogenic blackbody sources in our test optics. During the scan, a large number of pixels observe the same position in the field, and any given pixel crosses a large number of positions. This redundancy allows an independent determination of the gain and offset for each pixel, provided there are no short-time fluctuations in the illumination of the field, which can be excluded by

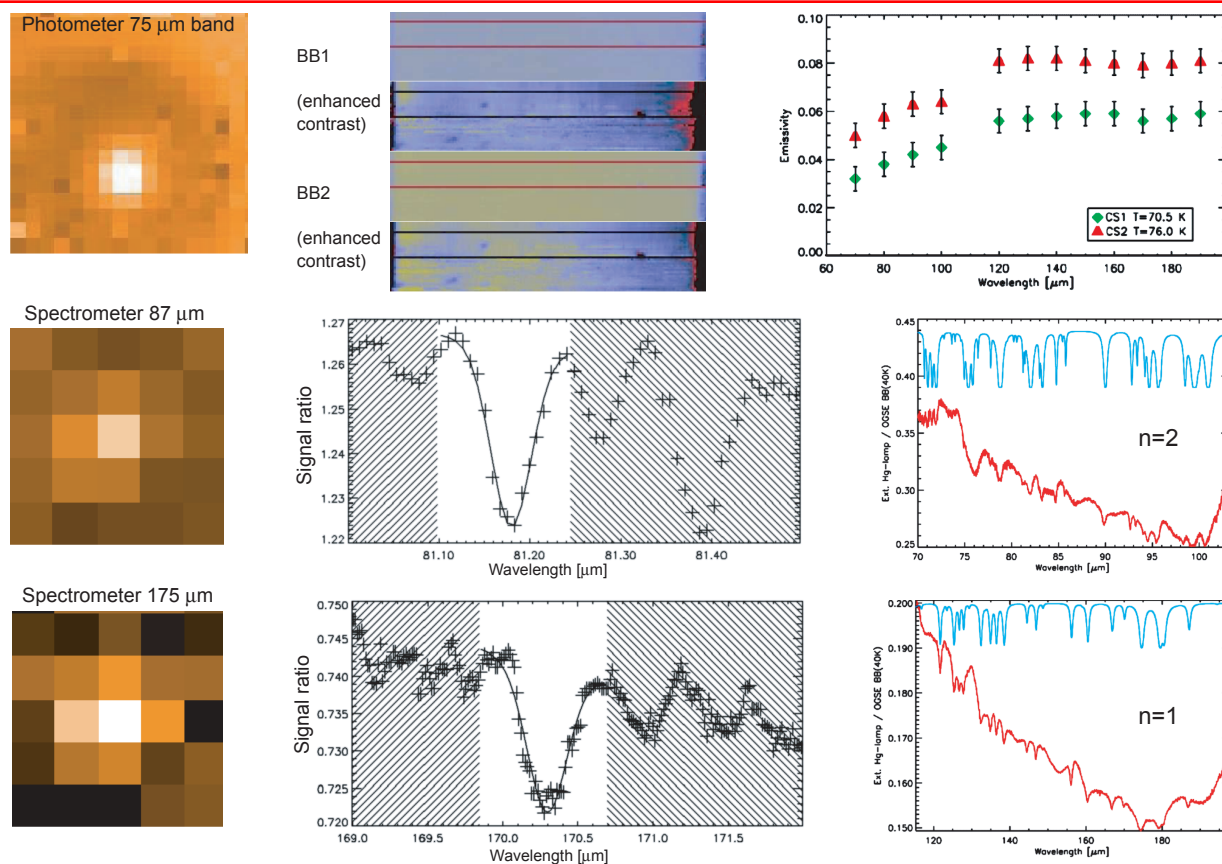


Figure 5. *Left column: Observations of a hole mask in front of a hot blackbody source in the nominal focus of the PACS telescope simulator optics. Top: Image on one subarray in the 75 μ m photometer band. Middle: Image on the spectrometer IFU created from the collapsed 87 μ m spectra of the corresponding detector modules in the unstressed photoconductor array. Bottom: Image on the spectrometer IFU created from the collapsed 175 μ m spectra of the corresponding detector modules in the stressed photoconductor array. Top center: Scanned observation of the full astronomical photometer field of view, which is illuminated by one of two cryogenic blackbody sources at a time. The scanning is done with the instrument chopper. Shown in this figure are the reconstructed images from these scans. When the dynamic range of the images is reduced to a narrow window, structures become visible, some of which are common to both sources, indicating some inhomogeneity in the optics (e.g. filters). Top right: Measured emissivity of the instrument-internal calibration sources which have been designed to approximately mimic the nominal telescope background. Middle center: Oversampled spectral scan (single spectrometer pixel) of an atmospheric water line in the second grating order. Middle right: Simulated (HITRAN2001) absorption spectrum of the laboratory atmosphere (upper trace) and observed spectrum of an external hot blackbody in the lab, divided by the spectrum of the cryogenic blackbody in vacuum, in the second grating order. Bottom center: Oversampled spectral scan (single spectrometer pixel) of an atmospheric water line in the first grating order. Bottom right: Simulated (HITRAN2001) absorption spectrum of the laboratory atmosphere (upper trace) and observed spectrum of an external hot blackbody in the lab, divided by the spectrum of the cryogenic blackbody in vacuum, in the first grating order.*

the long thermal time constant of our sources. The results (Fig. 5, top center) prove that the method works as anticipated, but they also reveal some weak structure in the apparent illumination of the field. The same, small spots are seen against both blackbody sources; this means they cannot come from the sources themselves; the fact that they appear in this chopper-scanned observation means they must originate in the optical path between the chopper and the source, e.g., from filter/mirror near a focus position. For astronomical observations of (faint) sources in the presence of the bright telescope background, this has the strong implication that even chopped/nodded observations are likely to confuse celestial structure with imperfections in the optics train; some scheme of rastering or line scanning with the telescope will probably turn out to be necessary for all observations

to distinguish true structure from artefacts.

4.3. Calibration Sources

The emissivity as a function of wavelength has been determined for both instrument-internal calibration sources (Fig. 5, top right). The design value was 4% which is approximately reached by Calibration Source 1 while Calibration Source 2 shows a significantly higher emissivity. With this information, the FM sources have been built such that we expect their emissivity to be close to the nominal value.

4.4. Spectrometer Resolution and Spectral Calibration

The very limited instrument test period did not allow dedicated, optimized measurements for a full characterization of the spectrometer; instead, available data from observations of the external, hot blackbody source through ~ 20 cm of laboratory atmosphere (Fig. 5, lower right four panels) were used to derive the resolving power and to test the precision of the angular resolver in the grating mechanism. Only lower limits could be derived for the resolving power; in the second grating order at $81\mu\text{m}$ we obtain $R > 1500$ (nominal: $R = 2100$), in the first grating order at $170\mu\text{m}$ we obtain $R > 550$ (nominal: $R = 1360$). A simple model spectrum has been calculated for a pressure of 1 bar, 45% humidity and a path length of 20 cm. The molecular data of H_2O and all its isotopes have been taken from the HITRAN2001 data base.¹³ Line by line optical depths pressure broadening and pressure induced lineshifts have been calculated for composing the respective Voigt profiles. The result has then been convolved with a gaussian instrumental profile of the predicted resolution of PACS for the respective wavelength range. This model spectrum has been used as input for a fit of the free parameters of the grating mechanism (optical angles vs. resolver units). One set of parameters and the Littrow equation were found to correctly describe the full observed wavelength range within the accuracy of the measurement ($< 1/3$ resolution element), in agreement with the specified accuracy of the resolver.

5. SYSTEM PERFORMANCE PREDICTION

Based on the results from the QM Instrument Level Tests and our tests of FM components/subunits and our present knowledge of the Herschel satellite, the performance of the entire system can be estimated in terms of what the observer is concerned with, i.e., an assessment of what kind of observations will be feasible with Herschel/PACS, and how much observing time they will require.

The system sensitivity of the instrument at the telescope depends mainly on the optical efficiency, i.e. the fraction of light from an astronomical source arriving at the telescope that actually reaches the detector, on the photon noise of the thermal background radiation from the telescope or from within the instrument, and on detector/electronics noise.

5.1. Optical Efficiency

The system optical efficiency has been modeled to the following level of detail:

- *Telescope efficiency:* The fraction of the power of a point source in the central peak of the point spread function is modeled in terms of absorption/obstruction, diffraction, and geometrical wave front errors ($6\mu\text{m}$ r.m.s.), which have been assumed to occur as spherical aberration.
- *Chopper:* Errors/jitter in the chopper throw and the duty cycle ($> 80\%$) are considered.
- *Mirrors and filters:* scatter/absorption losses – excluding diffraction – on each reflection by a mirror (1%) and efficiencies of filters/dichroics (as measured for the QM filters) are taken into account.
- *Diffraction:* An end-to-end diffraction analysis with the physical optics package GLAD 4.5 has been carried out for the spectrometer, where the image slicer is the most critical element of the PACS optics,^{14,15} and a simplified analysis for the less critical photometer as well as the effect of diffraction/vignetting by the entrance field stop and Lyot stop have been included.
- *Grating efficiency:* The grating has been analysed and optimised with a full electromagnetic code;¹⁴ the validity of this code has been confirmed by FTS measurements on a grating sample made by the manufacturer of the FM grating.

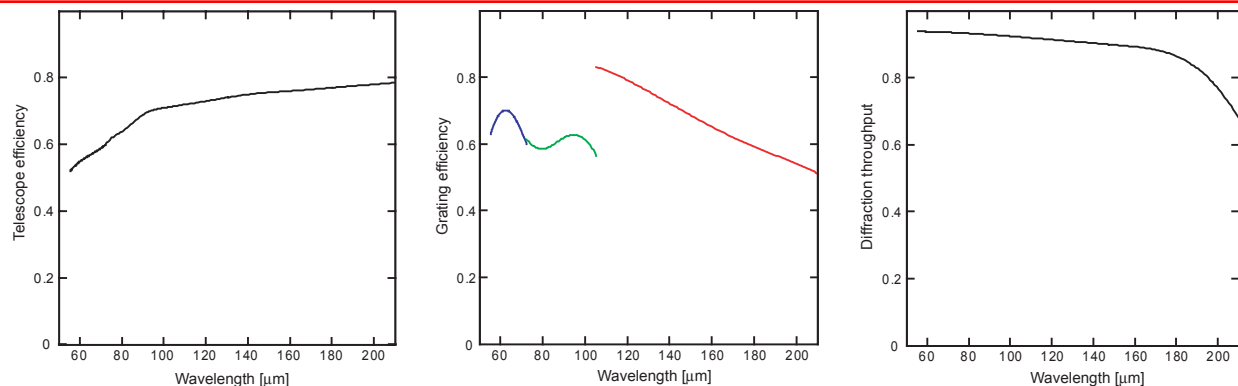


Figure 6. Optical efficiencies. Left: Telescope (main beam) efficiency for an assumed wave front error of $6\mu\text{m}$ r.m.s. Center: Calculated grating efficiency. Right: Diffraction throughput of the spectrometer optics; the diffraction losses mainly occur in the image slicer.

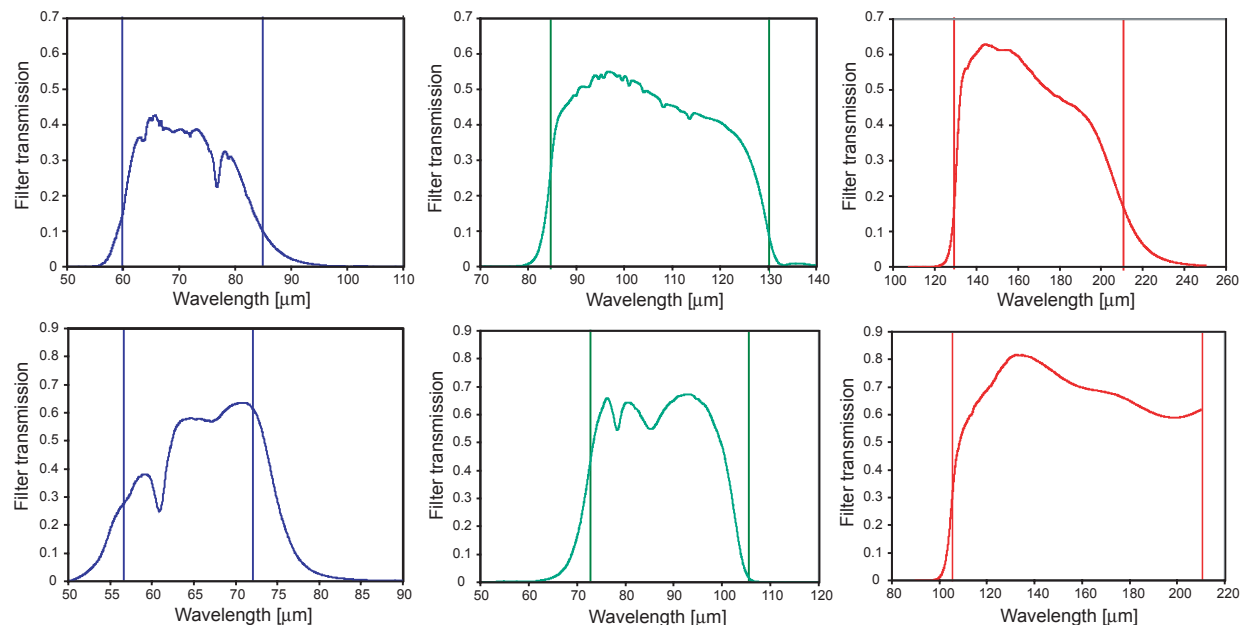


Figure 7. Filter transmission of the FM filters. The graphs represent the overall transmission of the combined filters in each branch of the instrument. The nominal band limits are indicated by the vertical lines. Top left: $60\text{--}85\mu\text{m}$ photometer band. Top center: $85\text{--}130\mu\text{m}$ photometer band. Top right: $130\text{--}210\mu\text{m}$ band. Bottom left: $57\text{--}72\mu\text{m}$ spectrometer band. Bottom center: $72\text{--}105\mu\text{m}$ spectrometer band. Bottom right: $105\text{--}210\mu\text{m}$ spectrometer band. Note: some FM filters have been replaced, with a potential for improvement of the transmission in the shortest wavelength bands of the photometer and the spectrometer.

5.2. Detectors

The NEP of the Ge:Ga photoconductor system is calculated over the full wavelength range of PACS based on the CRE noise and peak quantum efficiency determination at detector module level for the high-stress detectors. For the low-stress detectors we assume the same peak quantum efficiency. The quantum efficiency as a function of wavelength for each detector can be derived from the measured relative spectral response function. The achievable in-orbit performance depends critically on the effects of cosmic rays, in particular, high-energy protons. We have performed proton irradiation tests at the synchrotron source of the Université Catholique de Louvain (Louvain

la Neuve, Belgium) on stressed and unstressed detector modules under reasonably realistic conditions in terms of proton flux and energy, FIR background, and metallic shielding by the cryostat. A preliminary analysis of the results indicates that, with optimized detector bias settings and modulation schemes (chopping + spectral scanning), NEPs close to those measured without irradiation can actually be achieved;¹⁶ we, therefore, make the optimistic assumption that this will also apply to the actual conditions encountered in space.

For the bolometers, we use the NEPs measured at subunit level for both, the “blue” and “red” focal planes under realistic photon background.

5.3. Image Quality and Point Spread Function

The photometer optics – by design – delivers diffraction-limited image quality (Strehl ratio $\geq 95\%$). This has been verified by visible-optical measurements of the (geometrical) spot sizes during alignment. The (defocused) PSF measurements of the QM instrument do not contradict this. We therefore assume that the instrument optics will only contribute in a negligible way to the dilution of the central peak of the telescope PSF. This assumption will be verified during the FM instrument level tests with the (corrected) telescope simulator.

5.4. System Sensitivity

For the calculation of the system sensitivity we have included our present best knowledge of all components in the detection path as described above. The results for photometry and spectroscopy are shown in Fig. 8

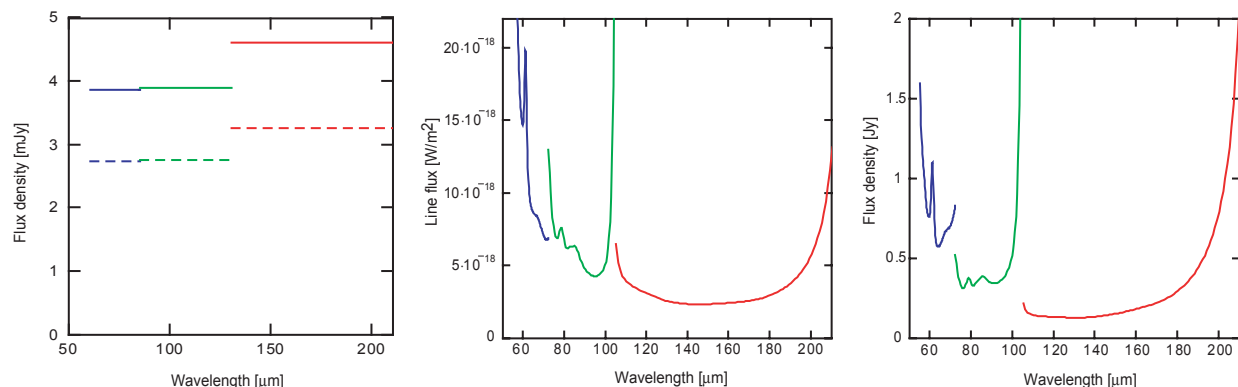


Figure 8. Sensitivity ($5\sigma/1h$ of integration) of the PACS instrument on Herschel for point source detection in photometry mode (left) and spectroscopy mode (center + right). For spectroscopy we distinguish between line detection, where we assume that the astronomical line is unresolved at the respective resolving power of the instrument (center), and continuum detection where the quoted sensitivity is reached for each spectral resolution element over the instantaneous spectral coverage of the instrument. The solid lines represent chopped observations where only half of the integration time is spent on the source. The dashed lines represent modulation techniques like on-array chopping or line scans where the source is on the array all the time.

It needs to be stressed that these figures must be considered preliminary, since no instrument level tests of the Flight Model have been carried out at the time of this writing. In some areas (e.g. short wavelength filters) we may foresee some improvement for the FM compared to the achieved performance used in the system model, in other areas, in particular, the behavior of the photoconductors under cosmic ray irradiation in the Herschel cryostat, predictions seem less reliable, and more severe adjustments of the sensitivity may occur after the satellite has reached its orbit.

ACKNOWLEDGMENTS

This work is supported by the following funding agencies: ASI (Italy), BMVIT (Austria), CEA/CNES (France), DLR (Germany), ESA-PRODEX (Belgium), and CDT (Spain).

REFERENCES

1. A. Poglitsch, C. Waelkens, and N. Geis in *IR Space Telescopes and Instruments*, J. Mather, ed., *Proc. SPIE* **4850**, pp. 662–673, 2003.
2. A. Poglitsch, C. Waelkens, O. H. Bauer, J. Cepa, T. F. Henning, C. van Hoof, R. Katterloher, F. Kerschbaum, D. Lemke, E. Renotte, L. Rodriguez, P. Royer, and P. Saraceno in *Optical, Infrared, and Millimeter Space Telescopes*, J. C. Mather, ed., *Proc. SPIE* **5487**, pp. 425–436, 2004.
3. S. Kraft, O. Frenzl, O. Charlier, T. Cronje, R. O. Katterloher, D. Rosenthal, U. Groezinger, and J. W. Beeman in *UV, Optical, and IR Space Telescopes and Instruments*, J. B. Breckinridge and P. Jakobsen, eds., *Proc. SPIE* **4013**, pp. 233–243, 2000.
4. S. Kraft, P. Merken, Y. Creten, J. Putzeys, C. van Hoof, R. O. Katterloher, D. Rosenthal, M. Rumitz, U. Groezinger, R. Hofferbert, and J. W. Beeman in *Sensors, Systems, and Next-Generation Satellites V*, H. Fujisada, J. B. Lurie, and K. Weber, eds., *Proc. SPIE* **4540**, pp. 374–385, 2001.
5. D. Rosenthal, J. W. Beeman, N. Geis, U. Groezinger, R. Hoenle, R. O. Katterloher, S. Kraft, L. W. Looney, A. Poglitsch, W. Raab, and H. Richter in *Proceedings FIR, Submm & mm Detector Technology Workshop*, J. Wolf, J. Farhoomand, and C. McCreight, eds., *NASA/CP- 211408*, 2002.
6. A. Poglitsch, R. Katterloher, R. Hoenle, J. Beeman, E. Haller, H. Richter, U. Groezinger, N. Haegel, and A. Krabbe in *Millimeter and Submillimeter Detectors for Astronomy*, T. Phillips and J. Zmuidzinas, eds., *Proc. SPIE* **4855**, pp. 115–128, 2003.
7. O. Charlier in *UV, Optical, and IR Space Telescopes and Instruments*, J. B. Breckinridge and P. Jakobsen, eds., *Proc. SPIE* **4013**, pp. 325–332, 2000.
8. Y. Creten, P. Merken, J. Putzeys, and C. van Hoof in *Proceedings FIR, Submm & mm Detector Technology Workshop*, J. Wolf, J. Farhoomand, and C. R. McCreight, eds., *NASA/CP- 211408*, 2002.
9. P. Agnese, C. Buzzi, P. Rey, L. Rodriguez, and J.-L. Tissot in *Infrared Technology and Applications XXV*, B. F. Andresen and M. S. Scholl, eds., *Proc. SPIE* **3698**, pp. 284–290, 1999.
10. P. Agnese, C. Cigna, J.-L. Pornin, R. Accomo, C. Bonnini, N. Colombel, M. Delcourt, E. Doumayrou, J. Lepennec, J. Martignac, V. Reveret, L. Rodriguez, and L. Vigroux in *Millimeter and Submillimeter Detectors for Astronomy*, T. Phillips and J. Zmuidzinas, eds., *Proc. SPIE* **4855**, pp. 108–114, 2003.
11. F. Simoens, P. Agnese, A. Béguin, J. Carcey, J.-C. Cigna, J.-L. Pornin, P. Rey, A. Vandeneynde, L. Rodriguez, O. Boulade, J. Lepennec, J. Martignac, E. Doumayrou, V. Reveret, and L. Vigroux in *Millimeter and Submillimeter Detectors for Astronomy II*, J. Zmuidzinas, W. S. Holland, and S. Withington, eds., *Proc. SPIE* **5498**, pp. 177–186, 2004.
12. L. Duband and B. Collaudin *Cryogenics* **39**, pp. 659–663, 1999.
13. L. S. Rothman, A. Barbe, D. C. Benner, L. R. Brown, C. Camy-Peyret, M. R. Carleer, K. Chance, C. Clerbaux, V. Dana, V. M. Devi, A. Fayt, J.-M. Flaud, R. R. Gamache, A. Goldman, D. Jacquemart, K. W. Jucks, W. J. Lafferty, J.-Y. Mandin, S. T. Massie, V. Nemtchinov, D. A. Newnham, A. Perrin, C. P. Rinsland, J. Schroeder, K. M. Smith, M. A. H. Smith, K. Tang, R. A. Toth, J. Vander Auwera, P. Varanasi, and K. Yoshino *JQSRT* **82**, pp. 5–44, 2003.
14. A. Poglitsch, C. Waelkens, and N. Geis in *Infrared Spaceborne Remote Sensing VII*, M. S. Scholl and B. F. Andresen, eds., *Proc. SPIE* **3759**, pp. 221–233, 1999.
15. L. Looney, W. Raab, A. Poglitsch, and N. Geis *ApJ* **597**, pp. 628–643, 2003.
16. R. Katterloher, L. Barl, A. Poglitsch, P. Royer, and J. Stegmaier in *Millimeter and Submillimeter Detectors and Instrumentation for Astronomy III. Proceedings of the SPIE, Volume 6275, paper 42 (2006)*, J. Zmuidzinas, W. S. Holland, S. Withington, and W. D. Duncan, eds.